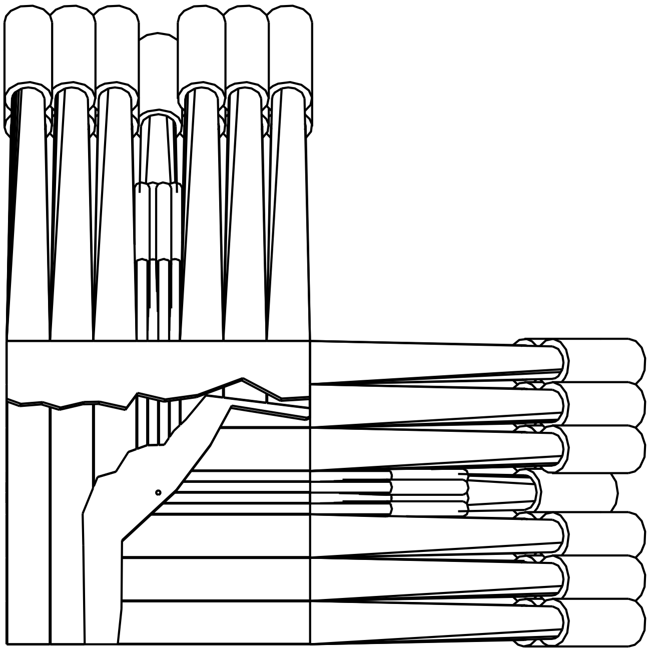

Figure 10: Front view of the of the presampler. Each slice in $x$ and $y$ corresponds to a different channel, with a finer granularity in the central region.

The position measurement is done in the same way as for the presampler with the $\sim 25\,\mathrm{X}_0$ depth being integrated in the same readout strip channel. A finer spatial resolution in the central region would not be needed here; assuming the same granularity as in the presampler, the calorimeter has 12 separated channels (6 for each side), leading to a total number of 28 channels, for the presampler and the main calorimeter.

Quartz-fibre calorimeters have achieved energy resolutions of $\sim 25\,\%/\sqrt{E} + 3\,\%$ [17] for a lead:fibre volume ratio of 4:1. Due to the numerical aperture of the fibres, the photostatistic contributed in this case to half of the stochastic term. Lowering the sampling ratio reduces the stochastic term by increasing the photostatistic and by reducing sampling fluctuations. The optimisation of the energy resolution part originating from the sampling fraction term will be investigated by detailed simulations and measured on prototypes. Furthermore, it has been shown [17] that the constant term can be made to vanish by arranging fibres in planes instead of the staggered geometry used in the above-mentioned prototype.

# 4 Electron taggers

The luminosity increase in the upgraded HERA is achieved by an earlier separation of the e and p beams. For this purpose the HERA magnet elements close to H1 are moved, which means that the Electron Tagger positions must be newly adjusted. The determination of optimal positions for the taggers and the study of their acceptances has been performed using the fast Monte Carlo (MC) simulation package H1LUMI [19] upgraded to take into account the future beam optics.

The present status of the new magnet layout near the IP is given in fig. 11. Electron tracing made according to this layout shows (fig. 12) that it is reasonable to place taggers between the end of the cold magnet BG and the horizontal focusing quadrupole QI2. The requirement of compactness is absolutely essential for these taggers.

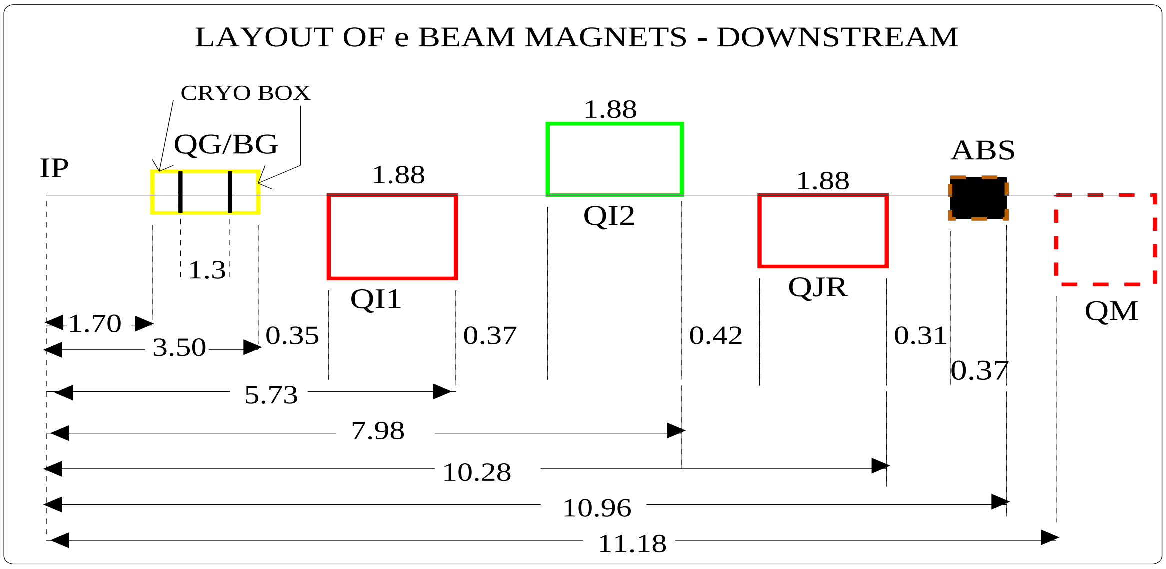


Figure 11: Upgraded HERA magnet layout near the IP (distances are in m).

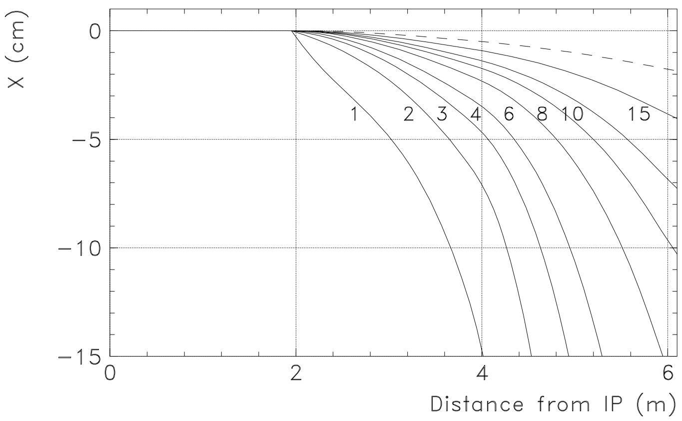


Figure 12: The trajectories of electrons with energies from 1 GeV to 27.5 GeV downstream of the IP (dashed curve corresponds to 27.5 GeV).

**ET6**

The only place for an electron calorimeter is the gap between magnets QI1 and QI2. As is seen in fig. 13 the accelerator beam pipe inside the quadrupole QI1 can be widened to allow for an exit window with a lateral length $\sim 8\,\mathrm{cm}$ for recoil electrons at the downstream edge of QI1 (5.7 m from IP). Behind the exit window it is planned to install the ET6: a Compact

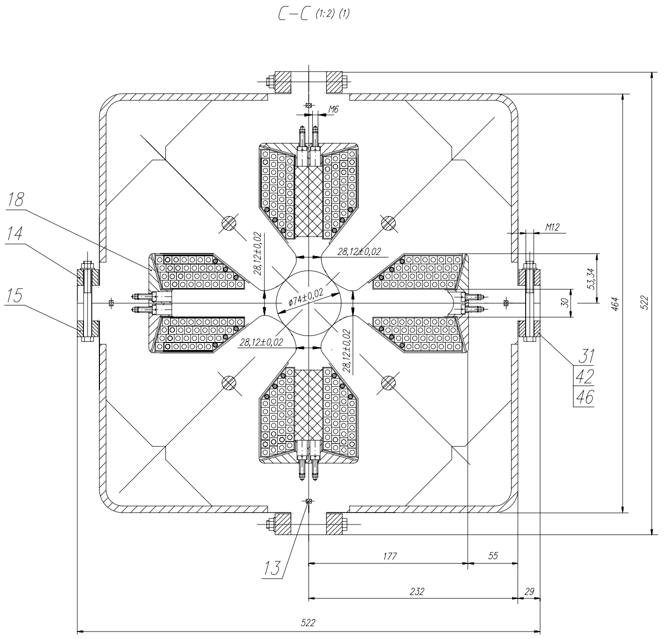


Figure 13: Cross section of QI1 quadrupole with the horizontal gap for the beam pipe.

Tungsten Calorimeter (CTC). CTC is a SpaCal type calorimeter, containing scintillating fibres of 0.5 mm in diameter with a filling coefficient of $\sim 25\,\%$ (W:Fibre ratio of 4:1). It is characterised by a small Molière radius of $\mathrm{R_M} \simeq 1\,\mathrm{cm}$ and $\mathrm{X_0} \simeq 0.7\,\mathrm{cm}$. An energy resolution better than $10\,\%/\sqrt{E/\,\mathrm{GeV}}$ is expected.

The MC simulation shows (fig. 14a) that recoil electrons stay within the vertical size of $y_{\mathrm{e}'} = \pm 1.5\,\mathrm{cm}$ from the e beam axis for ET6 position near the beam pipe of 4 cm radius. This gives the recommended thickness of 4 cm for CTC. Its optimal lateral length is determined by the $x_{\mathrm{e}'}/E_{\mathrm{e}'}$ correlation plot (fig. 14b) as 8 cm. The plot illustrates that the precise coordinate measurement is necessary for good energy reconstruction for those events which hit the detector near the boundary, where sizable leakage of the electromagnetic shower occurs.

Thus ET6 with a size of $4\times 8\times 15\,\mathrm{cm}^3$ will cover the whole available space and provide maximum possible acceptance for photo-production events. Good spatial resolution, allowing the determination of the electron impact point with precision $\sim 1\,\mathrm{mm}$, can be achieved with energy readout from different parts of the detector. As option a preshower made of CTC elements with vertical fibre alignment is also considered for improved space resolution. The readout will be performed using photomultipliers (PM). A light calibration system is also foreseen, to monitor the PM response and the light transmission in the fibres.

The energy distribution of electrons accepted by the CTC, given in fig. 14c, stems from the process of particle production by quasi-real photons with $Q^2 < 0.01\,\mathrm{GeV}^2$. The distribution covers an electron energy range from 6 to $11 - 14\,\mathrm{GeV}$, depending on the minimum distance of the CTC inner edge to the e beam axis. The ET6 acceptance distributions for these minimum distances are shown in fig. 14d. The corresponding energies of quasi-real photons will lie in the interval $11 - 20\,\mathrm{GeV}$, allowing the study of photo-production processes at $\langle W_{\gamma p}\rangle \sim 220\,\mathrm{GeV}$. Thus, after the HERA upgrade the ET6 will provide approximately the same conditions as

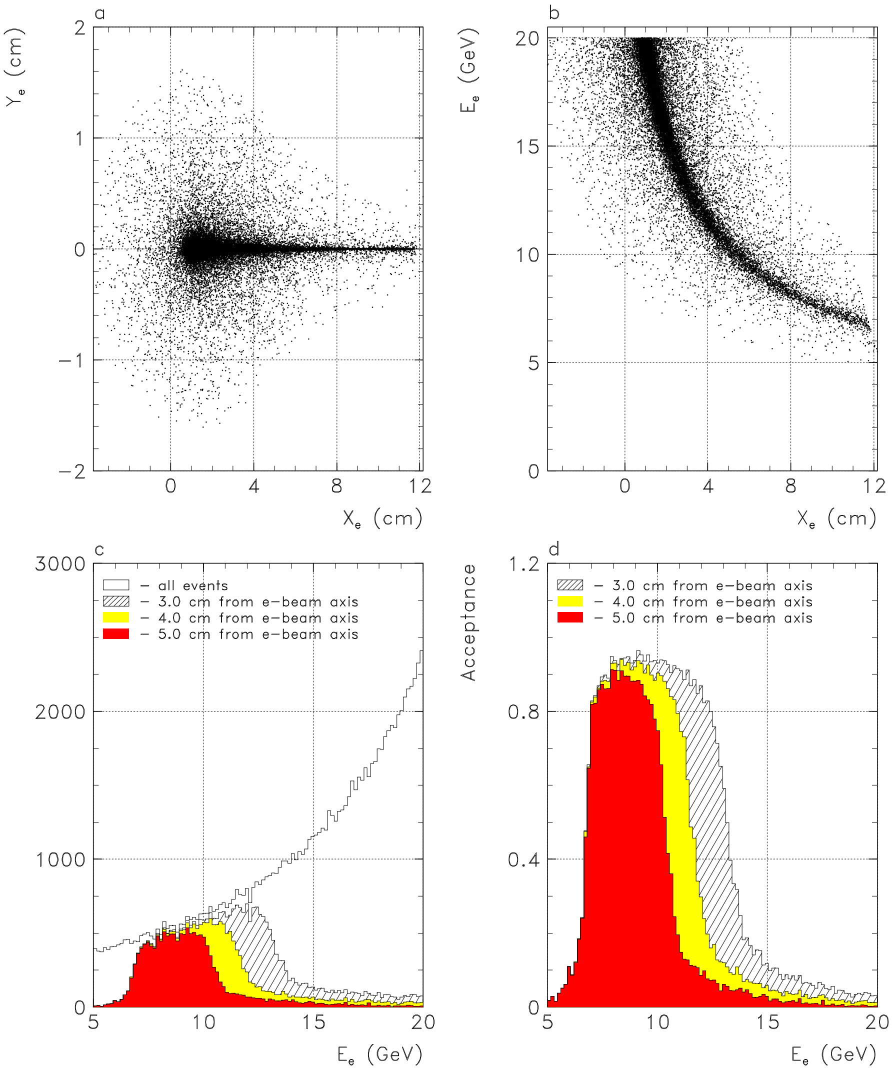


Figure 14: Scatter plot (a), correlation plot (b), events *vs* energy distribution of electrons (c) and acceptance (d) for ET6 .

the present ET33.

**ET44**

Since the future HERA magnet system stays almost unchanged at distances > 30 m from IP the tagger ET44 can be effectively used also after the HERA upgrade. The constituent KRS crystals have been replaced by NBW ($NaBi(WO_4)_2$) crystals for the 1998-1999 run period. The use of scintillating PWO ($PbWO_4$) crystals in ET44 to have better energy resolution (this is important for more precise acceptance determination) is under discussion. MC simulation performed for the new magnet lattice predicts approximately the same ET44 acceptance (fig. 15) as for the present HERA layout [20].

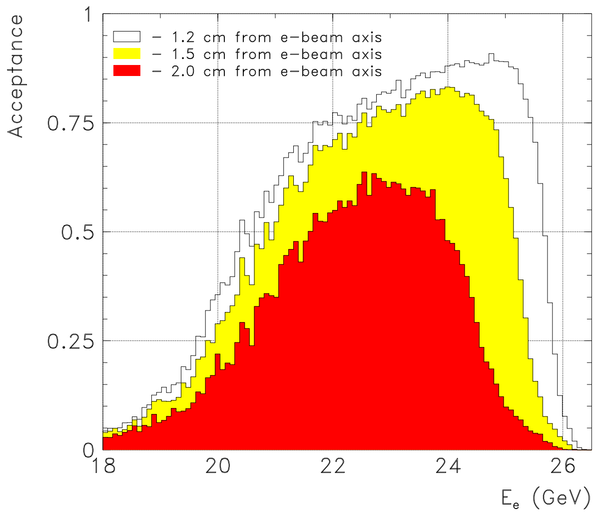


Figure 15: The results of acceptance simulation for ET44 for different positions of taggers relative to the e-beam axis.

Table 2 summarises the visible photo-production cross-sections in both Electron Taggers as function of their distances from the electron beam axis.

| d(cm) | ET6 | d(cm) | ET44 |
|---|---|---|---|
| 3.0 | 0.898 $\mu$b | 1.2 | 5.17 $\mu$b |
| 4.0 | 0.615 $\mu$b | 1.5 | 3.90 $\mu$b |
| 5.0 | 0.420 $\mu$b | 2.0 | 2.19 $\mu$b |

Table 2: Visible photo-production cross sections for electron taggers placed at different distances (d) from the electron beam axis.

The ability to require a detected electron/positron in the final state of high ET jet production and heavy flavour production will be important both in defining efficient triggering and for the best possible kinematic reconstruction of such processes.

## 5 Electronics

The general electronics layout is shown in fig. 16. This scheme is designed for both photon and electron detectors. It would also be a suitable solution for the upgrade of the polarimeter readout.

Basically, the calorimetric chain consists of a fast analog shaping, a 12 bit ADC providing 4 energy samples per bunch and a dedicated fast readout by a commercial processor (Power PC) which performs on-line histogramming at a high rate ($\sim$ 1 MHz). The analysis of the